European Journal of Mechanics / B Fluids 94 (2022) 90–105

Contents lists available at ScienceDirect

European Journal of Mechanics / B Fluids

journal homepage: www.elsevier.com/locate/ejmflu

Tornados and cyclones driven by Magneto-hydrodynamic forces

Abdellah Kharicha [a,*], Mohamad Al-Nasser [a], Hadi Barati [a], Ebrahim Karimi-Sibaki [a], Alexander Vakhrushev [a], Mehran Abdi [a], Andreas Ludwig [b], Menghuai Wu [b]

[a] Christian Doppler Laboratory for Metallurgical Applications of Magnetohydrodynamics, Franz-Josef Street 18, 8700 Leoben, Austria
[b] Chair for Modeling and Simulation of Metallurgical Processes, Department of Metallurgy, Montanuniversität, Franz-Josef Street 18, 8700 Leoben, Austria

ARTICLE INFO

Article history:
Received 9 June 2021
Received in revised form 28 January 2022
Accepted 1 February 2022
Available online 16 February 2022

Keywords:
Tornado
Cyclones
Electro-vortex
Weather hazards
Liquid metal batteries
Hall–Héroult process
Electric arc furnaces
Vortex breakdown

ABSTRACT

A numerical analysis is carried out to explore the variety of flow structures induced inside a conducting fluid emerging from the interaction of an electric current source with an external axial magnetic field. Results are obtained for Shercliff (S) numbers up to 10^{10} and Hartmann (Ha) numbers up to 115, for a single magnetic Prandtl number of $P_m = 8.6 \times 10^{-7}$. Depending on these numbers, very different swirling flow patterns are predicted. Transitions seem to be solely controlled by two dimensionless ratios $\Gamma = Ha/(PmS)^{1/2}$ and $N = Ha^6\ Pm/S$.

For low Γ, vortex-breakdown, tornados and cyclones are obtained. These MHD tornados are found to be very similar in structure to atmospheric tornados. A slight increase in Γ results in the transformation of the tornado into a cyclone which rotates at relatively constant angular velocity. Surprisingly for further increase in *Ha*, the cyclone is restructured into an inverted tornado. The induced currents are found to be at the origin of this phenomenon. For large *N*, a Hartmann swirling flow occurs which is associated with almost vertical electric current lines. In this regime, both poloidal and azimuthal flows are damped, and remain mainly present in the forcing region at the edge of the electric current column. These results may be of relevance for the understanding of flow structures in the atmosphere, in aluminum reduction cells, electro-metallurgical processes, and in liquid metal batteries.

1. Introduction

The combined use of electric current sources and axial magnetic field is a popular method to generate swirling Magneto-hydrodynamic(MHD) flows [1]. Radial current interacts with an axial magnetic field to drive the flow in the tangential direction. Depending on the magnitude of the current and the magnetic field, different laminar and turbulent flow phenomena were observed.

Based on literature, phenomena can be differentiated into two very different groups depending on the intensity of applied current and axial external magnetic field.

In the first group, low current (<10 A) and high magnetic field (>0.1T) were used to study instabilities in electrolytes and liquid metals. Using electrolytes Antar et al. [2] and Pérez-Barrera et al. [3,4] investigated new instabilities in which leads to the formation of traveling anticyclone vortices. In liquid metals, induced currents can reach a similar magnitude to the applied one. Sommeria et al. [5,6] injected low current in a thin liquid mercury layer in the presence of external axial magnetic field. In presence of a relatively high external magnetic field, the applied current was solely constricted to flow in the Hartmann layer and inducing an electrical azimuthal vortex. Messadek et al. [7] studied experimentally the MHD shear layer and the importance of Hartmann layer in turbulence and energy dissipation. The study covered a wide range of current and intensive axial magnetic field up to 6 T. Strong poloidal damping, restructuration of the main flow, and a two-dimensional turbulence aligned with the magnetic field were observed [5,7]. When a mechanically driven swirling flow is subjected to axial magnetic fields, the Lorentz force brakes the radial velocity and so the poloidal field [8–10]. If the magnitude of the magnetic field is sufficiently high, the Ekman layer resulting from the equilibrium between the centrifugal and viscous forces is replaced by the Hartmann layer expressed by an equilibrium between electromagnetic and viscous forces [8,9]. If the magnetic field magnitude exceeds a critical value, numerical studies have shown that the poloidal hydrodynamical vortex breakdown is suppressed by the magnetic field [10–13]. Kharicha et al. [12] have shown the existence of an electromagnetic vortex breakdown built by the poloidal induced electric current lines. No clear correlation in shape and position was found between this new electromagnetic vortex and the hydrodynamical one [13].

* Corresponding author.
E-mail address: Abdellah.kharicha@unileoben.ac.at (A. Kharicha).

https://doi.org/10.1016/j.euromechflu.2022.02.001
0997-7546/

In the second group, strong current (>100 A) with low magnetic field(<10 mT) have attracted the attention of many researchers working on industrial processes such as electroslag remelting process [14,15], electric arc furnaces [16–18], aluminum reduction cells [19] and liquid metal batteries [20]. In these processes, current up to 10^5A are used to heat or to promote electrochemical transfer at electrolyte–metal boundaries. Physically, when a sufficiently strong current is applied through a conducting material, a poloidal flow known as Electrovortex (EVF) emerges from the Lorentz force resulting from the interaction between the electric current and its self-magnetic field. Depending on the medium and the electric current density, these forces can lead to negligible secondary flows up to potent electro-vortex jets. One of the first studies on EVF in liquid metal was performed by Shercliff [21] which predicted the formation of electro-vortex flow (EVF) when concentrated current passes through liquid metals. For very high current and small electrodes, Bojaverics et al. [22] observed experimentally the apparition of swirl. The presence of the earth magnetic field was assumed to be the origin of the tangential driving of the flow. Kharicha et al. [23] confirmed through numerical simulation of the Bojarevics' s experiment that small magnetic fields like the earth magnetic field are capable of inducing strong swirling flow, despite a ratio of 1 to 100 between tangential and poloidal Lorentz forces. In another study, Kharicha et al. [24] performed an experimental and numerical study on a liquid metal cylindrical container to analyze the effect of MHD. In the study, it was observed that a small external magnetic field can significantly affect the flow pattern inside the liquid metal. A tornado was generated at the axis of symmetry. Several further studies have confirmed the extreme sensitivity of the electro-vortex on the applied axial magnetic field magnitude [25,26]. K. Liu et al. [27] compared experimental measurements of an EVF, with simulations. Good agreement was achieved only if the presence of a small axial magnetic field was assumed to be present. The study concluded that external magnetic fields alters and damps the flow as the field increases. This mechanism of poloidal electro-vortical flow suppression in an electro-vortex flow has been verified in a liquid metal experiment performed by Kolesnichenko et al. [28]. They showed for the first time the important role of the centrifugal forces in counteracting the Lorentz forces.

Herreman et al. [29] studied the effect of electro-vortex flows inside liquid metal batteries in single and multiphase fluid systems. Herreman et al. [30], evaluated the impact of external magnetic field inside liquid metal batteries during discharge at high rate ≈ 1–10 kA. The study showed that a low axial magnetic field 1–10 mT allows efficient mixing of the liquid alloy. A 2D axisymmetric simulation in additions to 3D DNS (Direct Numerical Simulation) simulations was conducted. The results showed that both simulation trials lead to similar magnitudes of velocity.

Strong vortical flow patterns were also obtained in a non-axisymmetric configuration by Kenjereš [31]. It consisted in combining a horizontal DC electric current over an arrays of permanent magnets. The MHD generated turbulence was found to greatly enhance the heat transfer at walls.

From the aforementioned literature, it is clear that extremely different flow structures may develop depending on both intensities of the applied current and imposed magnetic field. Interestingly, all of these flows show a strong tendency in 2D or 3D axis symmetricity. Herein, we present a 3D axisymmetric MHD model. The 3D electromagnetic field is solved with only 2 equations, the induction and the magnetic potential in the tangential direction. For a specific cylindrical geometry, we explore the swirling flows generated by a wide range of applied currents and axial magnetic field magnitudes.

2. Model

In this study, the physical configuration resembles a 3D axisymmetric model consisting of a cylindrical electrically conducting bath in direct contact with a solid and a liquid electrode. The applied current enters the domain from the top boundary (top electrode), and leaves it from a small bottom electrode. The electric current density is assumed uniform at the bottom boundary of the small electrode (Fig. 1). All other boundaries are considered to be electrically insulated. The interface with the top liquid electrode is assumed flat and steady. The poloidal applied current generates a self-magnetic field in the azimuthal direction. An external axial magnetic field of intensity B_{Z0} is applied. The insulator and the electrode region are included in the computational domain to simplify the boundary conditions for the magnetic potential equation. The dimensions of the domain are taken such that the ratio of the electrodes radius, as well as the electrode to the height of the domain is 1 to 5. The aspect ratio of the present geometry is the same as the one used in liquid metal batteries by Herreman et al. [29]. Fig. 1(a) represent the 3D geometry, and Fig. 1(b) illustrates the domain composed of three regions: the electrically conducting liquid, electrode, and non-conducting enclosure. The mesh consists of 220,000 finite volume elements.

2.1. Governing equations

The flow inside the conducting liquid is treated as an isothermal flow. In addition to the continuity and Navier–Stokes, the induction equations are solved in cylindrical coordinates to predict the electric current density and magnetic fields. The effect of the turbulence is estimated with the SAS-SST K-omega model [32].

The fluid flow equations are described by the continuity and Navier–Stokes equations:

$$\nabla \cdot \vec{u} = 0, \tag{1}$$

$\vec{u}$ is the fluid velocity vector field.

$$\rho \frac{\partial \vec{u}}{\partial t} + \rho \vec{u} \cdot \nabla \vec{u} = -\nabla p + \mu \nabla^2 \vec{u} + \vec{J} \times \vec{B}, \tag{2}$$

p, ρ, μ, $\vec{J}$, $\vec{B}$ stand for pressure, density, effective viscosity, electric current density, and magnetic field, respectively. Assuming axisymmetric condition, the electromagnetic problem can be solved solely from the tangential component of the magnetic field B_θ, and the magnetic potential vector A_θ.

$$\frac{\partial B_\theta}{\partial t} + \vec{u} \cdot \nabla B_\theta = \frac{1}{\sigma \mu_0} \nabla^2 B_\theta + \frac{\partial}{\partial r}\left(\frac{B_\theta}{\sigma \mu_0 r}\right) - \frac{\partial}{\partial z}(u_\theta B_z) - \frac{\partial}{\partial r}(u_\theta B_r), \tag{3}$$

where σ is the electrical conductivity and μ_0 vacuum magnetic permeability.

The magnetic potential equation is needed to calculate the effect of applied axial magnetic field through solving A_θ equation to calculate B_z and B_r.

$$\sigma \frac{\partial A_\theta}{\partial t} + \sigma \vec{u}.\nabla A_\theta = \nabla\left(\frac{1}{\mu_0} \nabla A_\theta\right) + \frac{\partial}{\partial r}\left(\frac{1}{r \mu_0}\right) A_\theta - \sigma\left(\frac{u_r A_\theta}{r}\right). \tag{4}$$

The poloidal components of the electric current (J_r, J_z) can be extracted from the tangential magnetic field B_θ, while J_θ can be extracted solely from A_θ:

$$\vec{J} = \frac{1}{\mu_0} \nabla \times \vec{B} \rightarrow \begin{cases} j_r = -\dfrac{1}{\mu_0} \dfrac{\partial B_\theta}{\partial z} \\ j_\theta = -\sigma\left(\dfrac{\partial A_\theta}{\partial t} + u_z \dfrac{\partial A_\theta}{\partial z} + \dfrac{u_r}{r} \dfrac{\partial (r A_\theta)}{\partial r}\right) \\ j_z = \dfrac{1}{r \mu_0} \dfrac{\partial (r B_\theta)}{\partial r} \end{cases} \tag{5}$$

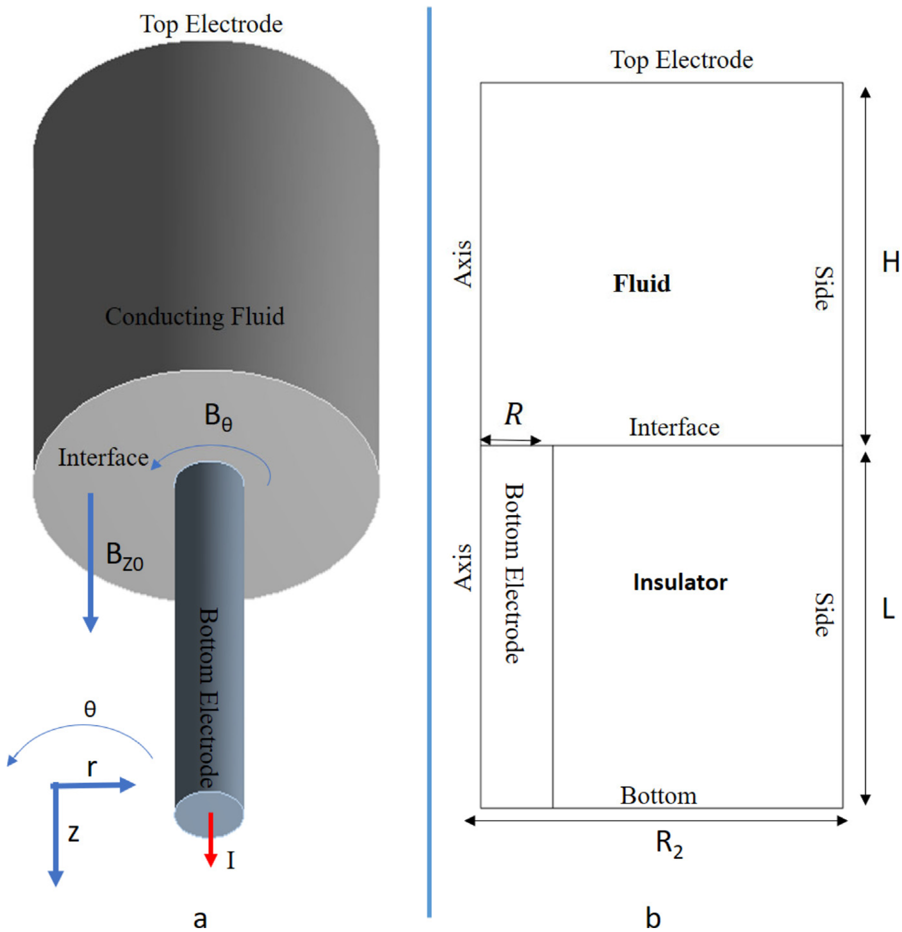

Fig. 1. (a) 3D view of domain. (b) Geometry of the 2D axisymmetric space: R = 1; H = L = R_2 = 5.

In the similar way the radial and axial component of the magnetic field can be extracted:

$$\vec{B} = \nabla \times \vec{A} \rightarrow \begin{cases} B_r = -\dfrac{\partial A_\theta}{\partial z} \\ B_z = \dfrac{1}{r}\dfrac{\partial (rA_\theta)}{\partial r} \end{cases} \tag{6}$$

The 3D components of the Lorentz force are then obtained by crossing the electric currents (J_r, J_θ, J_z) and magnetic field (B_r, B_θ, B_z) components.

To generalize the study, non-dimensionalization of the equations is performed to get a more general solution in accordance with dimensions of the physical domain. The following scales are considered for the non-dimensionalization [29]:

$$[l] = R;\ [t] = \frac{R^2\rho}{\mu};\ [u] = \frac{\mu}{R\rho};\ [p] = \frac{\mu^2}{\rho R^2};\ [B_\theta] = \frac{\mu_0 I}{2\pi R};$$
$$[A_\theta] = RB_{Z0} \tag{7}$$

Here, we distinguish between the self-induced magnetic B_θ induced by the applied current and the induced poloidal magnetic field (B_r, B_z) which is generated by the fluid motion in the presence of applied field B_{Z0} and imposed current.

I stands for the total applied electric current. For the sake of simplicity, the dimensionless symbols for the magnetic field and the magnetic potential are kept the same ($A_\theta, B_r, B_\theta, B_z$).

The dimensionless equations are:

$$\frac{\partial \vec{U}}{\partial t} + \vec{U}.\nabla\vec{U} = -\nabla P + \nabla^2\vec{U} + H_a\sqrt{\frac{S}{P_m}}(\vec{J}_{r,z} \times \vec{B}_{r,z})$$
$$+ S^2(\vec{J}_{r,z} \times \vec{B}_\theta) + \frac{H_a^2}{P_m}(\vec{J}_\theta \times \vec{B}_{r,z}) \tag{8}$$

$$\frac{\partial B_\theta}{\partial t} + \vec{U}.\nabla B_\theta = -\frac{H_a}{\sqrt{P_m S}}\left(\frac{\partial (U_\theta B_z)}{\partial z} + \frac{\partial (rU_\theta B_r)}{\partial r}\right) + \frac{1}{P_m}\nabla^2 B_\theta - \frac{B_\theta}{r^2 P_m} \tag{9}$$

$$\frac{\partial A_\theta}{\partial t} + \vec{U}.\nabla A_\theta = \frac{1}{P_m}\nabla^2 A_\theta - \frac{1}{P_m}\frac{A_\theta}{r^2} - \frac{U_r A_\theta}{r} \tag{10}$$

Dimensionless numbers H_a, S, P_m are defined as follows:

$$S = \frac{\mu_0 I^2}{4\pi^2\nu^2\rho};\quad H_a = B_{ext}R\sqrt{\frac{\sigma}{\mu}};\quad P_m = \frac{\sigma\mu_0\mu}{\rho} \tag{11}$$

S represents the ratio between the Lorentz force produced by the electric current source and viscous forces. The Hartmann number represents the ratio of Lorentz force produced by the induced current to viscous forces. S scales the effect of induced magnetic field on the system while H_a characterizes the effect of poloidal magnetic field. P_m is the magnetic Prandtl number.

2.2. Boundary conditions

The boundary conditions for B_θ and A_θ are applied at the external boundaries and at some internal boundaries. If we integrate radially the dimensionless form of the Ampere's law (Eq. (5)) over a horizontal surface section, we obtain a relation that can be used to define accurately the boundary condition for B_θ at the fluid/insulator interface:

$$\int_0^r \vec{J} \cdot d\vec{S} = \int_0^r \nabla \times \vec{B} \cdot d\vec{S} \rightarrow B_\theta(r) = \frac{1}{r}, \tag{12}$$

Table 1
List of boundary conditions for B_θ,A_θ and flow.

Boundary	B_θ	A_θ	Flow
Bottom electrode/Fluid			$U_z = U_r = U_\theta = 0$
Top electrode	$\frac{\partial B_\theta}{\partial z} = 0$	$\frac{\partial A_\theta}{\partial z} = 0$	$\frac{\partial U_r}{\partial r} = \frac{\partial U_\theta}{\partial r} = U_z = 0$
Interface (Fluid/insulator)	$B_\theta = \frac{1}{r}$		$\frac{\partial U_r}{\partial r} = \frac{\partial U_\theta}{\partial r} = U_z = 0$
Axis	$B_\theta = 0$	$A_\theta = 0$	$\frac{\partial U_z}{\partial r} = 0; U_r = U_\theta = 0$
Side wall	$B_\theta = \frac{1}{5}$	$A_\theta = \frac{5}{2}$	$U_z = U_r = U_\theta = 0$
Bottom walls	$\frac{\partial B_\theta}{\partial z} = 0$	$\frac{\partial A_\theta}{\partial z} = 0$	

where $d\vec{S}$ is a unit surface vector and r the radial coordinate of the electrically insulating boundary element. The expression Eq. (12) gives also the conditions $B_\theta = 0.2(r = R_2 = 5)$ at the side wall and $B_\theta = 1(r = R = 1)$ at the electrode/insulator (see Table 1).

The same kind of integration is operated on the Eq. (6) for A_θ until the radial position of the side wall:

$$\int \vec{B} \cdot d\vec{S} = \int \nabla \times \vec{A} \cdot d\vec{S} \rightarrow B_z \pi R_2^2 = 2\pi R_2 A_\theta (r = R_2)$$
$$\rightarrow A_\theta (r = R_2) = \frac{B_z R_2}{2}. \tag{13}$$

Numerically Eq. (13) gives $A_\theta (r = R_2) = \frac{5}{2}$ at the side wall. This integration assumes that inside the bath, the axial magnetic field does not deviate sensibly from the applied field (in dimensionless form $B_z \approx 1$). The two Ampere's laws (Eqs. (5)–(6)) also imply that $B_\theta = A_\theta = 0$ at the axis ($r = 0$). On horizontal top and bottom boundaries, the electromagnetic field is assumed to not change in the axial direction. $\frac{\partial B_\theta}{\partial z} = \frac{\partial A_\theta}{\partial z} = 0$. At the bottom electrode boundary, a uniform current density is automatically obtained by the use of $\frac{\partial B_\theta}{\partial z} = 0$ as boundary condition. The reason lies first in (a) the imposition of $B_\theta = 1$ at the electrode/insulator which forces the current to flow vertically, and (b) in the sufficiently long and uniformly conducting electrode (L = 5).

Slipping conditions are applied to the fluid/insulator interface and the top electrode. Non slipping conditions is applied to all other walls.

Boundary conditions for the flow and electromagnetic field are summarized in Table 1.

2.3. The Lorentz forces

The Lorentz force can be separated in three contributions: (1) $S^2\vec{J}_{r,z} \times \vec{B}_\theta$ drives the poloidal flow and generates the electro-vortex flow, (2) the Hartmann term $\frac{H_a^2}{P_m}\vec{J}_\theta \times \vec{B}_{r,z}$ is generated by the interaction of tangential induced currents with the poloidal magnetic field, it usually damps the poloidal fields. (3) $H_a\sqrt{\frac{S}{P_m}}\vec{J}_{r,z} \times \vec{B}_{r,z}$ is the source of angular momentum. In the present study, the flow slightly disturbs the applied axial magnetic field, the radial component remains much smaller than the axial component $B_r \ll B_z \sim 1$. However, the space–time variation of A_θ cannot be neglected, it describes the induced electric current J_θ in the tangential direction which will be responsible of the damping of the poloidal flow at high Hartmann numbers. The poloidal induced current can be divided in two parts, $\vec{U} \times \vec{B}_\theta$ and $\vec{U} \times \vec{B}_{r,z}$. They are included and "mixed" inside the B_θ equation (see Eq. (9)).

There is a physical separation between the poloidal and tangential magnetic fields, (B_θ) is directly influenced by the poloidal field ($B_{r,z}$). In contrast, (B_θ) influences the poloidal field indirectly through (U_r, U_z). The intensity of the electromagnetic coupling depends directly on the ratio $H_a/\sqrt{P_m S}$ (see Eq. (9)).

3. Numerical methods and validation

The equations are solved using a finite volume method. The mesh has been refined several time until no change in the solution number is achieved. Our investigation explores the coupling and interaction between two extreme MHD phenomena, the electro-vortical flows (High S, Ha = 0), and Hartmann flows (High Ha, low S). Thus, it is necessary to test these two extremes. The validations (Fig. 2) were successfully performed on the geometry and data of Herreman et al. [29] ($S \leq 10^6$, Ha = 0) and Sommeria [5] $S = 7$, Ha = 237). These two validations ensure that the two kinds of MHD (electro-vortical and Hartmann flows) are correctly predicted by our model.

4. Results

Simulations will cover the range $S = 10^2$–10^{10} for a Hartmann number up to 115. The magnetic Prandtl number is fixed to $P_m = 8.6 \times 10^{-7}$, a typical value corresponding to a moderately conducting liquid metal like iron.

In Figs. 2–13 results are given in term of electric current, Lorentz force, velocity and pressure fields. The resulting dimensionless poloidal and azimuthal velocities can be used to define Reynolds and Taylor numbers. We choose to define a Reynolds number based on the volume (V) average of the Poloidal kinetic energy:

$$\mathrm{Re}^2 = \frac{1}{2}\int (U_r^2 + U_z^2) dV / \int dV \tag{14}$$

And a Taylor number based on the volume average of the angular kinetic energy:

$$Ta^2 = \frac{1}{2}\int U_\theta^2 dV / \int dV \tag{15}$$

Evolutions of the (resulting) Reynolds and Taylor numbers are displayed in Figs. 11–12.

From the Reynolds and Taylor number, two magnetic Reynolds numbers can be calculated. A poloidal and angular magnetic Reynolds number can be obtained from the products P_mRe and $P_m Ta$. In the present study both remains smaller than 10^{-1}.

Outside the liquid domain the applied magnetic field is purely axial without radial component $\vec{B} = (B_r = 0, B_z = B_{Z0})$. Within the fluid, when the flow is strong enough the poloidal magnetic field can be bent $\vec{B}_{ext} = (B_r \neq 0, B_z \neq B_{Z0})$, and so a radial magnetic field comes into existence. This effect has been fully taken into account by the model. However, in the present study even for the largest S (strongest flow), the radial component B_r remains much smaller compared to the axial component. The reason lies in the fact that the poloidal magnetic Reynolds number remains much smaller than 1.

In Fig. 13, the flow pattern map reports the occurrence of rope tornado, tornado, cyclone, inverted tornado, and Hartmann flow for each of the explored (S, Ha) couple. For the sake of illustration, schematic of flow pattern exhibiting clear 3D structures are given in Fig. 14.

Before discussing the physical mechanisms in action, a short overview of these flow patterns is given from the lowest to the highest Ha values:

(1) *Electro-vortex flow:* close to the bottom electrode, a converging flow produces a powerful jet towards the top electrode (Fig. 3). The electric current lines enter the domain from the top anode electrode, and converges towards the

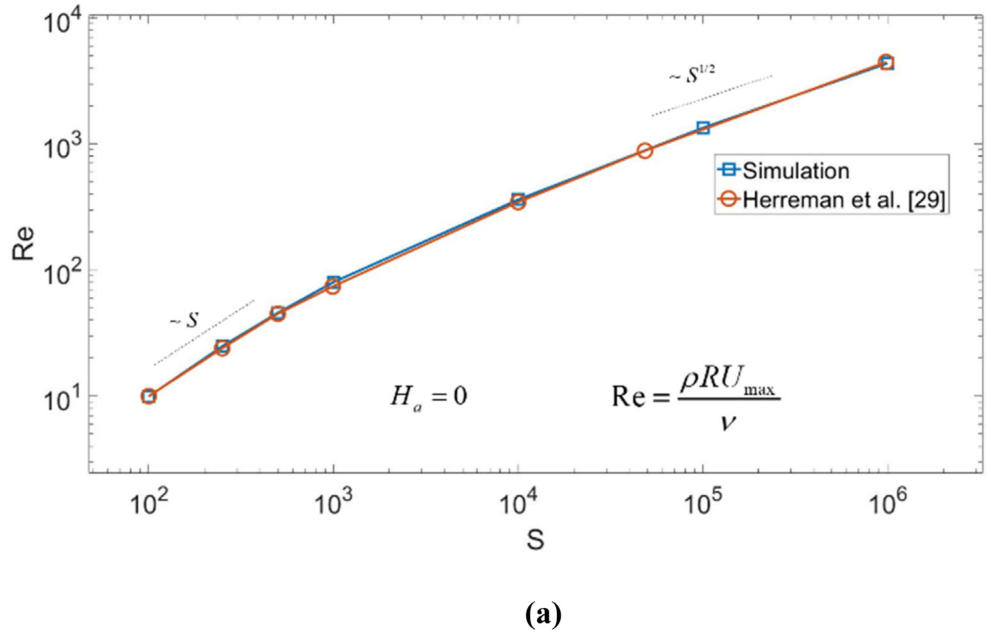

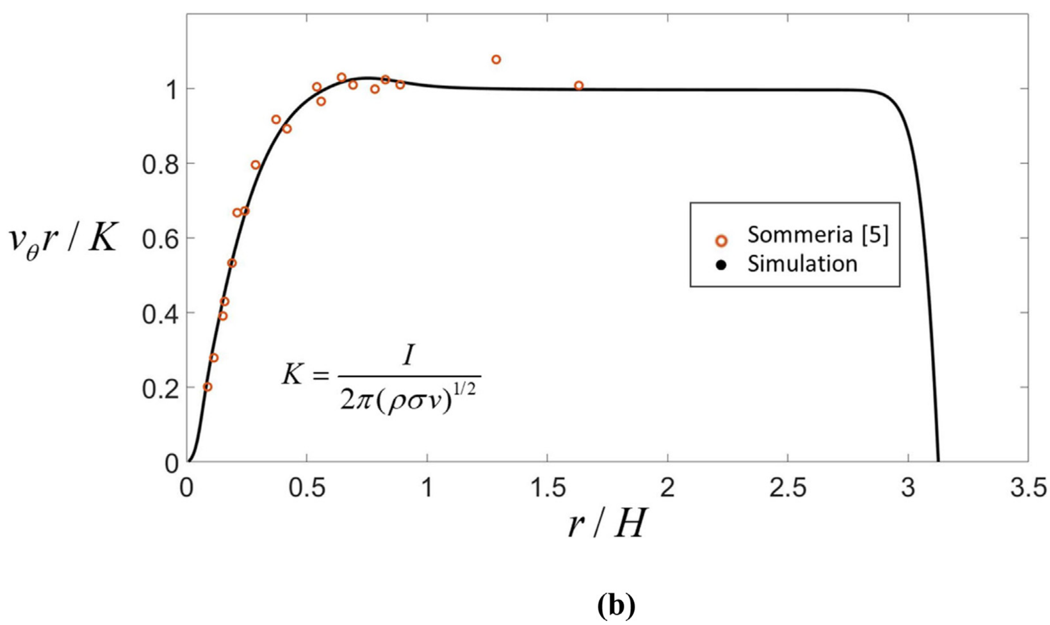

Fig. 2. Validation of the model (a) comparison with Herreman et al. [29] with H = 1; R = 0.2, R_2 = 1 for Ha = 0; (b) comparison with Sommeria [5] with H = 15.36, R = 1, R_2 = 48 for S = 6.86 and Ha = 237.

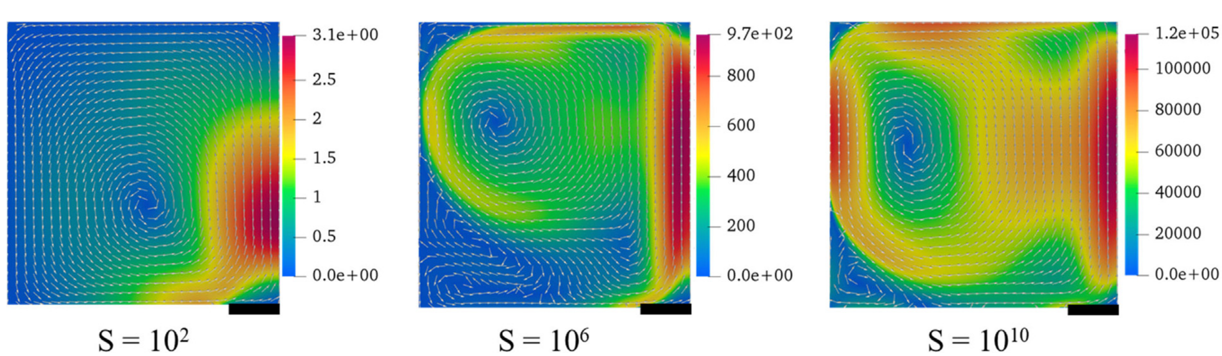

Fig. 3. Electro-vortex. Flow distribution for Ha = 0 for different value of *S*. Poloidal velocity vector field and magnitude. Position of the bottom electrode is marked in black.

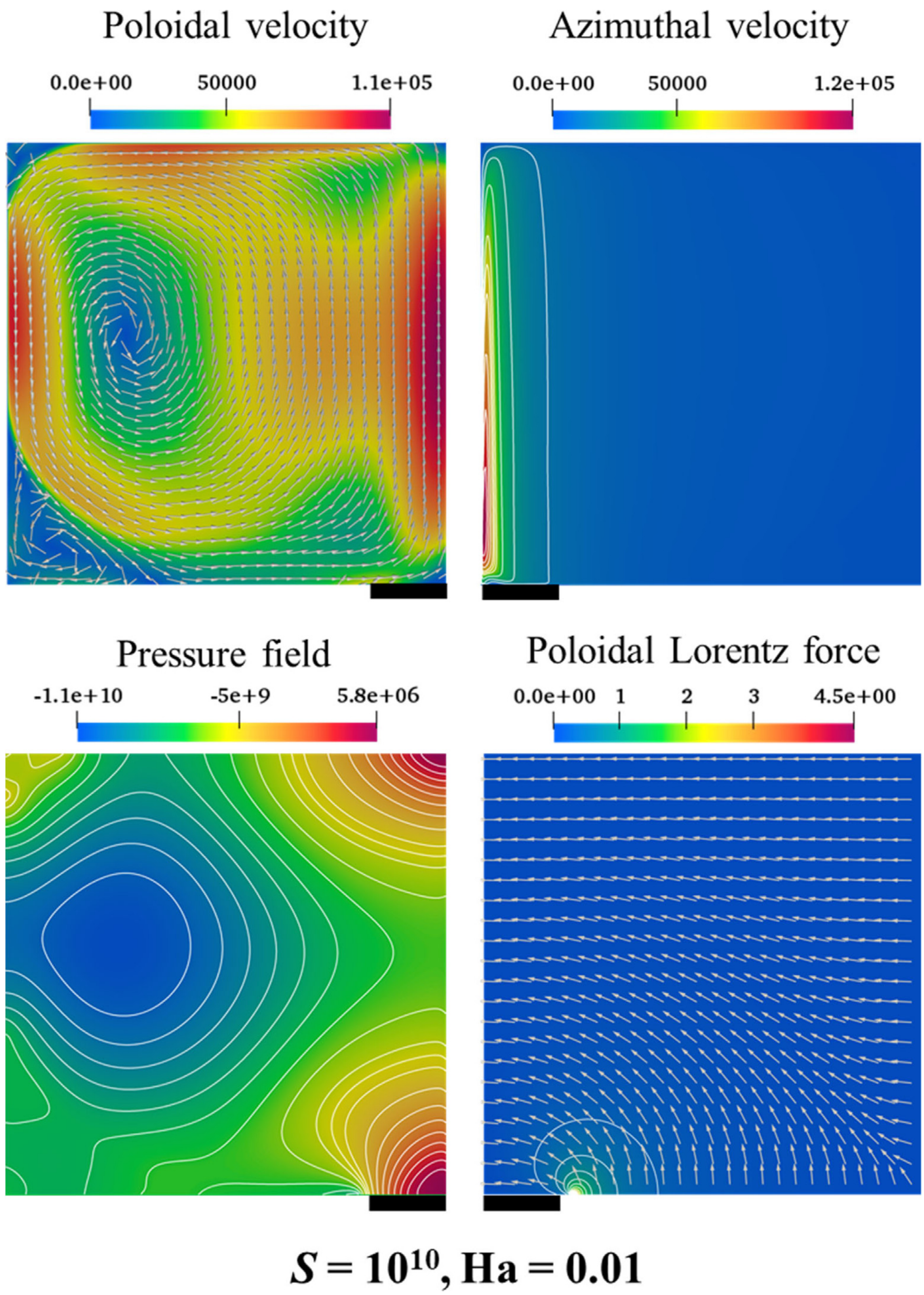

Fig. 4. Rope tornado ($S = 10^{10}$, Ha = 0.01).

small cathode at the bottom (Fig. 10). Through the Lorentz force, flow recirculation emerges all over the domain with a higher velocity near the axis. Due to the absence of any forces in the azimuthal direction, this flow is purely 2D.

(2) *Rope tornado and vortex breakdown*: Azimuthal velocity is concentrated at the axis of symmetry (Fig. 4) by the strong electro vortex flow. The length of the electro-vortex jet along the axis decreases with increasing magnetic field. At some Hartmann number, the rope tornado is interrupted by the apparition of a vortex breakdown. This poloidal vortex rotates in the opposite direction to the electro-vortex (Fig. 5).

(3) *Tornado*: The vortex breakdown further extends and pushes the electro-vortex out of the axis region. The surface of the tornado which is defined by the region of high swirl, is localized at the boundary between the electro-vortex and vortex breakdown. The vortex Breakdown occupies all the inside volume of the tornado, a downdraft flow hit the electrode (Fig. 6).

(4) *Cyclone*: For a sufficiently high magnetic field, the swirl forcing further opens the “mouth “of the tornado. The electro-vortex is pushed towards the top extremity; vortex breakdown occupies almost the entire volume. Compared to tornado, the entire volume rotates at relatively uniform angular velocity (Fig. 7). The maximum azimuthal velocity

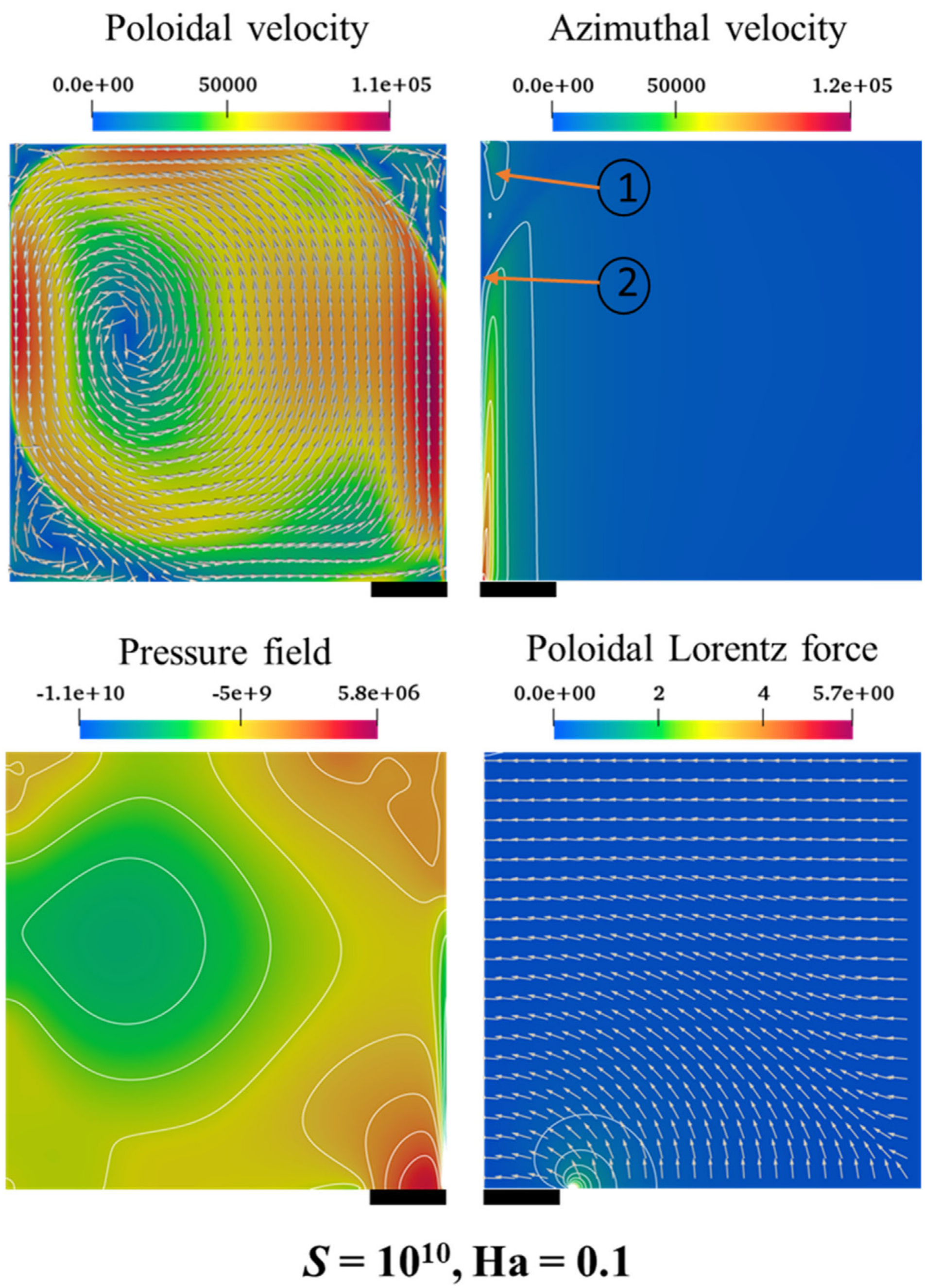

Fig. 5. Vortex breakdown development at the top of a rope tornado ($S = 10^{10}$, Ha = 0.1). (1) Vortex breakdown (2) Position at which the rope tornado is interrupted.

is located at a certain radius position. For the highest Hartmann numbers this position is located at the close vicinity of the lateral wall (Fig. 7). However even stronger angular velocities can occur locally close to the bottom and top boundary layers.

(5) *Inverted Tornado:* Within the heart of the cyclone, a new stable vortex breakdown appears near the bottom electrode. Here also the vortex breakdown extends all along the axis until reaching the upper boundary. This new vortex breakdown concentrates enough angular momentum to give birth to an inverted tornado within a still existent cyclone (Fig. 8).

(6) *Hartmann swirling flow:* For the highest Hartmann numbers, the poloidal flow is strongly damped. The azimuthal flow is mainly present in the forcing region and at the surface of the bath/insulator interface (Fig. 9).

5. Discussion and physical mechanisms

5.1. Scalings

The dynamic of this system can be understood by considering the equilibrium between 4 forces, the centrifugal force and three electromagnetic forces, i.e. the poloidal Lorentz force, the azimuthal Lorentz force and the Hartmann damping.

As previously mentioned, the intensity of the coupling between the poloidal and azimuthal magnetic fields is controlled by the ratio of applied to self-magnetic fields: $\Gamma = H_a/\sqrt{P_m S}$ (see Eq. (10)).

Without magnetic field the flow scales linearly with S for $S<10^3$, and with $S^{1/2}$ for $S>10^4$ (Fig. 2). In these scalings, the Lorentz forces are first balanced by the viscous stresses. For the larger Reynolds numbers they are balanced by the inertial forces.

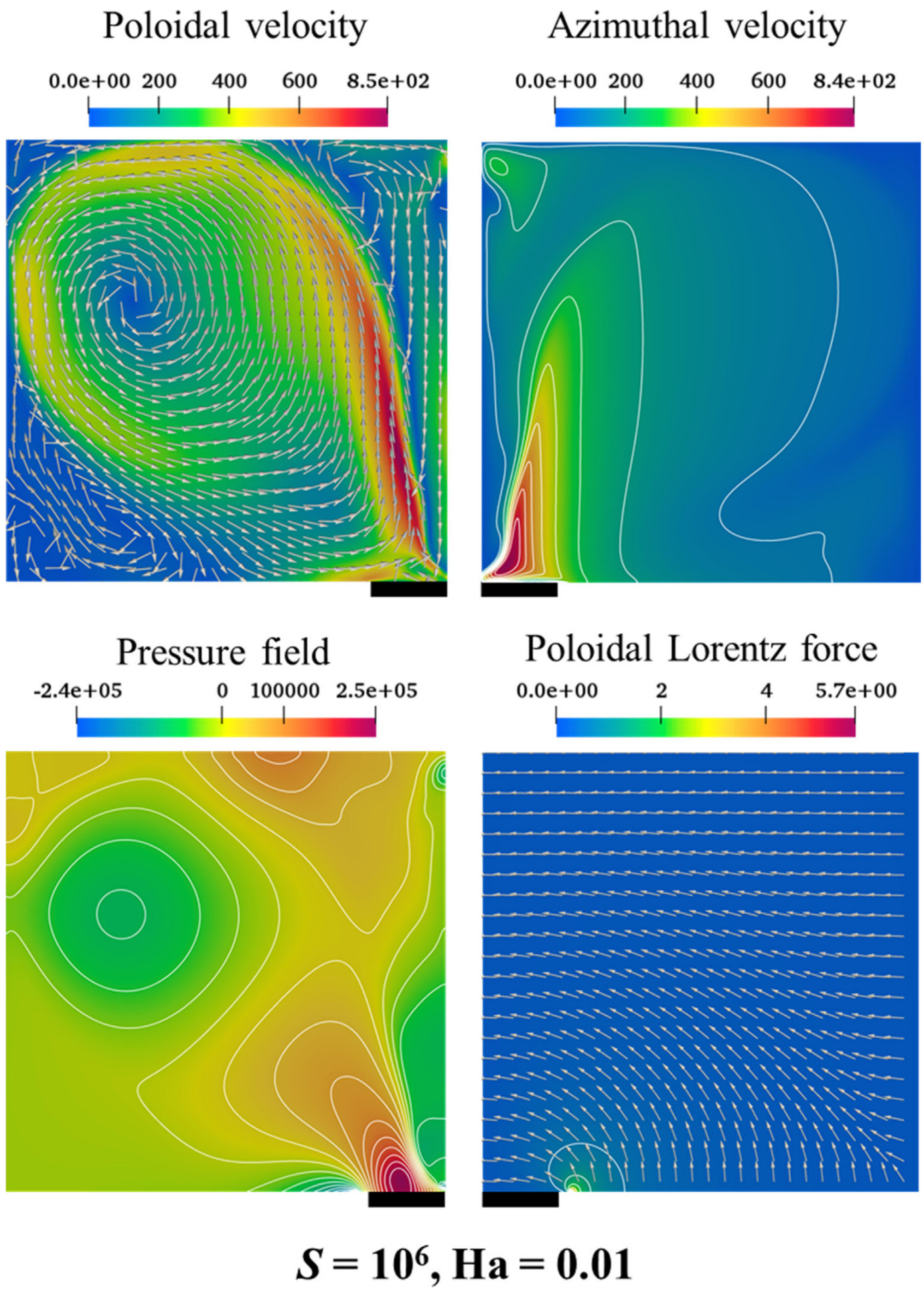

Fig. 6. Tornado ($S = 10^6$, $H_a = 0.01$).

(a) ***Low Ha numbers***

If a magnetic field is introduced, an equilibrium between the centrifugal force and the azimuthal Lorentz force can take place which leads to the following scaling for the azimuthal velocity:

$$\vec{U}.\nabla\vec{U} \sim H_a\sqrt{\frac{S}{P_m}}(\vec{J}_{r,z} \times \vec{B}_{r,z}) \Rightarrow U_\theta^2 \sim H_a\sqrt{\frac{S}{P_m}} \tag{16}$$

As shown in Fig. 12, this trend is relatively well respected by some of the data.

The ratio of fields Γ controls the transition between (1) the rope tornado and tornado with $\Gamma \approx 10^{-3}$ and (2) the transition between tornado and cyclones with $\Gamma \approx 10^{-2}$ (Fig. 13).

(b) ***High Ha numbers***

For high *Ha*, the azimuthal flow results from the equilibrium between the azimuthal forcing and the Hartmann damping:

$$H_a\sqrt{\frac{S}{P_m}} \sim \frac{H_a^2}{P_m}U_\theta \Rightarrow U_\theta \sim \frac{1}{H_a}\sqrt{\frac{S}{P_m^3}} \tag{17}$$

The term (1/Ha) predicts the saturation and a decrease of the azimuthal kinetic energy for large values of Ha (Fig. 12).

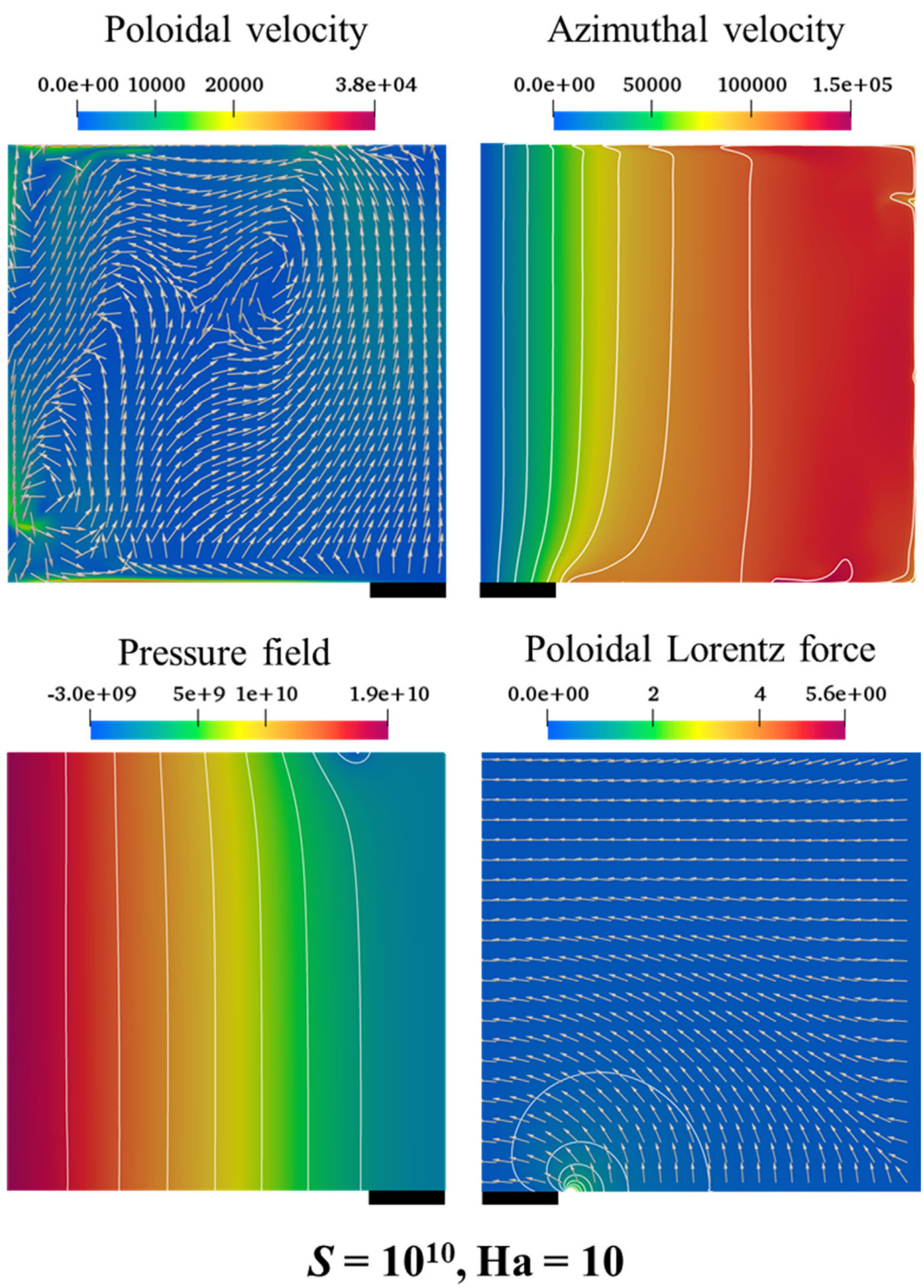

Fig. 7. Cyclone ($S = 10^{10}$, $H_a = 10$).

The radial momentum is driven by the equilibrium between the centrifugal force and the Hartmann damping force:

$$U_\theta^2 \sim \frac{H_a^2}{P_m} U_r \tag{18}$$

Based on (Eq. (17)), we can estimate a scaling for the radial velocity:

$$U_r \sim \frac{S}{P_m^2 H_a^4} \tag{19}$$

Which allows us to define a dimensionless poloidal interaction number:

$$N = \frac{H_a^2 U_r / P_m}{U_r^2} = \frac{H_a^6 P_m}{S} \tag{20}$$

The results show that the transition between cyclone/inverse tornado and the Hartmann swirling flow occurs clearly for N ~const ($S \sim H_a^6$) (Fig. 13). The transition between cyclone/inverse tornado flows deviates sensibly from N~const, the boundary seems to follow $S \sim H_a^{4.5}$.

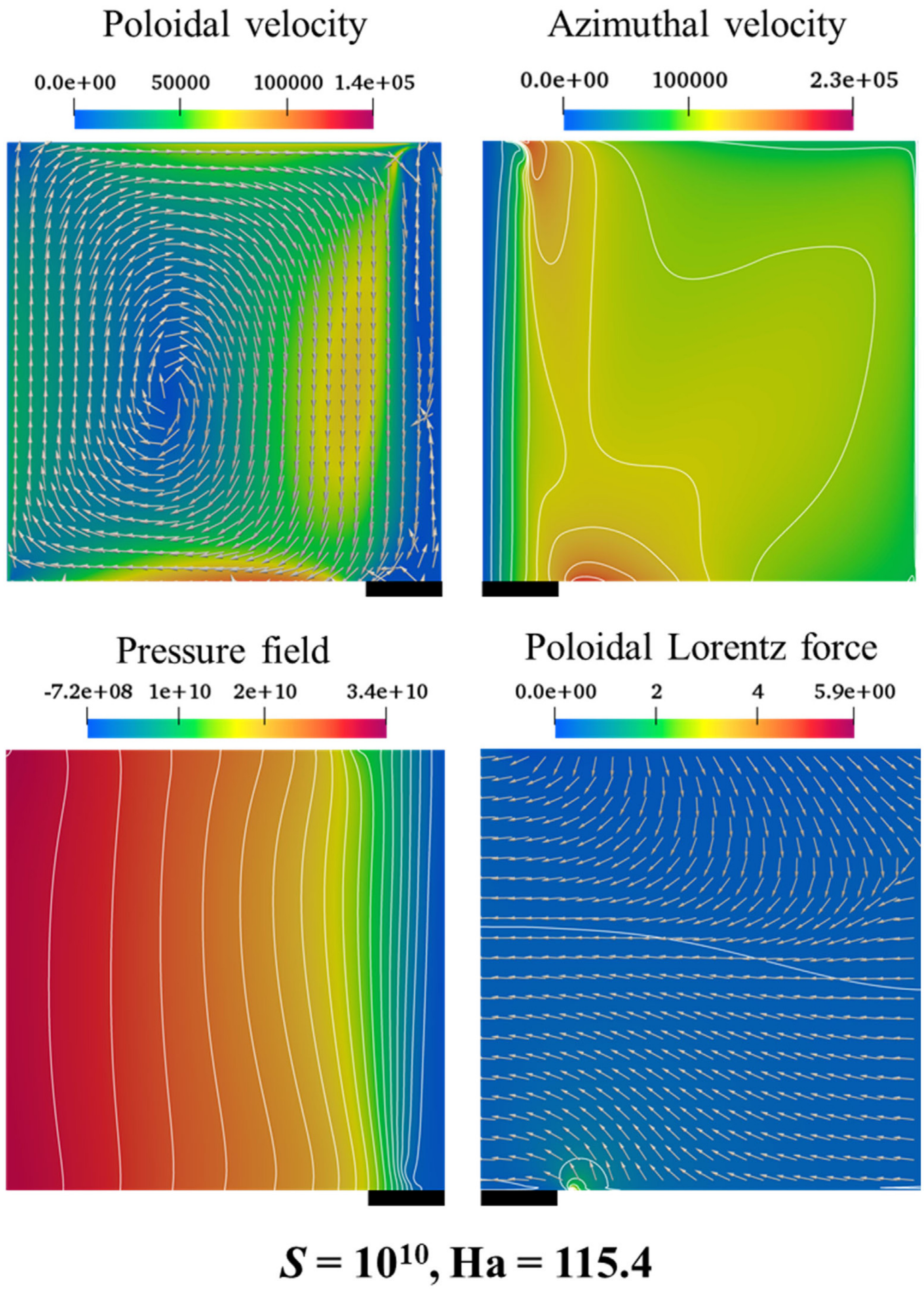

Fig. 8. Inverted tornado ($S = 10^{10}$, $H_a = 115.4$).

5.2. Physical mechanisms

For $Ha = 0$, the flow is driven by the electro-vortex. It basically emerges when a non-uniform electric current flows inside a conducting fluid. The current interacts with its self-induced magnetic field to create a Lorentz force that acts only in the radial and axial directions. This force drives a strong upward jet. Conservation of mass induces the global flow known as electro-vortex. This flow can be clearly observed in this study in the absence of external magnetic field (Ha = 0) and for very low ratio $\Gamma < 10^{-3}$ (Figs. 2, 4–6). The Lorentz force is dominantly acting radially inwards, and it scales with the square of applied current. At the bottom electrode, current is concentrated near the center that in turn generates the highest value of the force. This explains the strong jet that emerges in this area. The impact of the jet on the top of the domain creates the global vortex. Due to the absence of any forces in the azimuthal direction, the flow is purely 2D. The main flow and electric current densities show similar distribution along the whole range of S.

The presence of an external axial magnetic field makes the flow three dimensional. The radial currents interact with the axial magnetic field inducing a new Lorentz force which is the source of swirling. The angular momentum is then transported by the poloidal flow in the meridional plane.

For $\Gamma < 10^{-3}$, this transport leads to the apparition of a thin rope tornado resulting from the swirl confinement at the axis

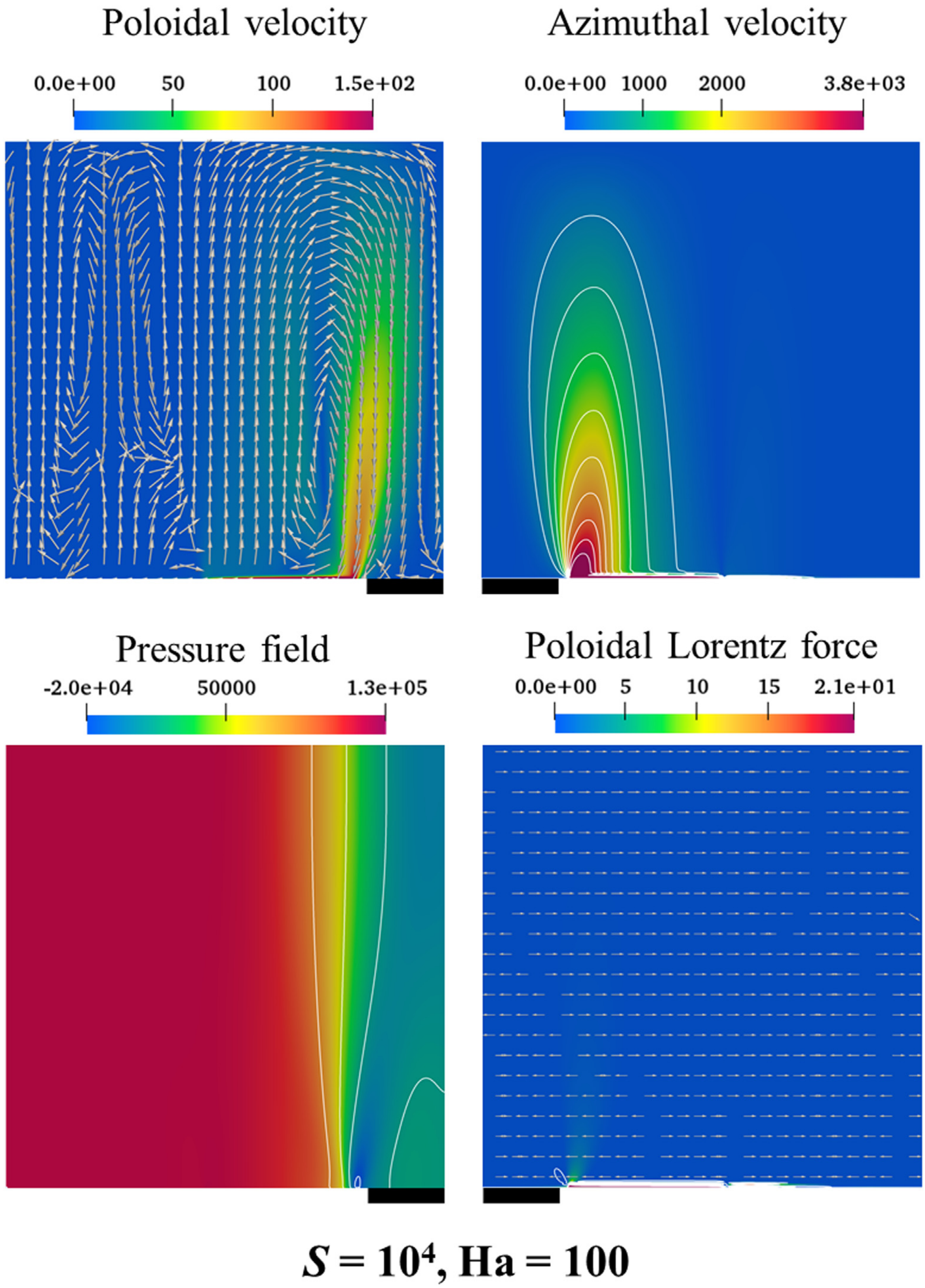

Fig. 9. Hartmann swirling flow ($S = 10^4$, $H_a = 10^2$).

(Fig. 4). With increasing Ha, a low pressure region develops along the vertical axis due to the centrifugal force. If the accumulated swirl is sufficiently high, the centrifugal force opens the rope tornado leading to the apparition of a vortex breakdown (Fig. 5). This vortex appears due to the opposite flow (downdraft in the picture) driven by the pressure gradient existing between the opening mouth of the rope tornado and the surrounding non-rotating fluid. The vortex breakdown occupies the upper part of the domain, where weaker swirl velocities are present and where the poloidal (electro-vortex) flow slows down [33,34].

In Vogt et al. [35] tornado-like structure was obtained with the combined use of rotating and traveling magnetic field. The use of a stronger traveling magnetic field was found to drive a converging poloidal flow that concentrates the angular momentum at the axis of the container. The traveling magnetic field in Vogt et al. [35] plays a similar role to the electro-vortex flow in the present study.

As the external magnetic field increases, the tangential MHD force enhances the centrifugal force at the tornado surface. This process strengthens the vortex breakdown which pushes the electro-vortex out of the axis region. It results in a widening of the tornado, V and trumpet shapes can be obtained.

For the range of $\Gamma\sim 10^{-3}$–10^{-2}. During the tornado regime, the electro-vortex is weakened by the apparition of the vortex breakdown, the poloidal kinetic energy decreases (Fig. 11). The centrifugal force counters the poloidal Lorentz forcing. The end

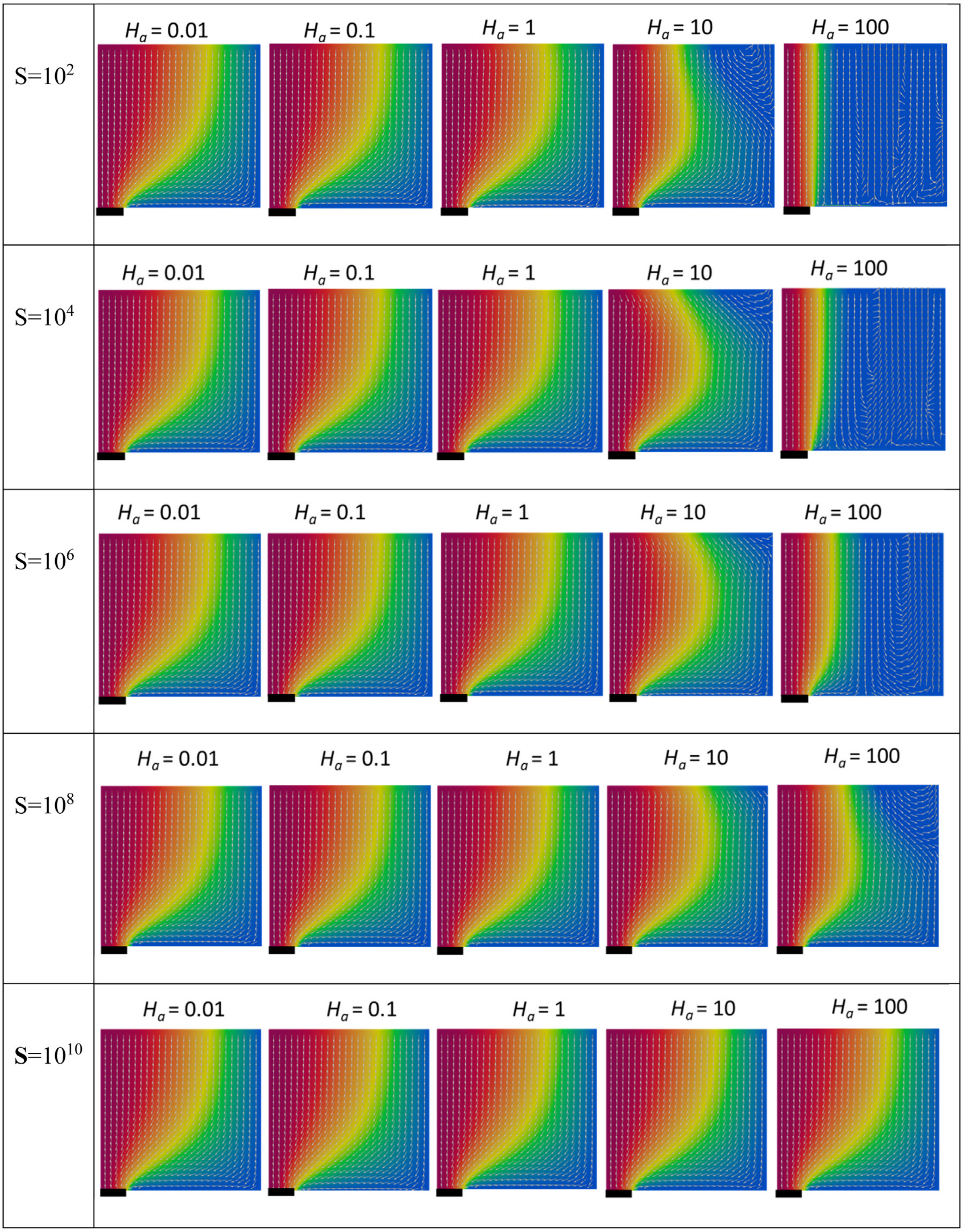

Fig. 10. Electric current lines.

of the tornado flow regime can be characterized by the extinction of the electro-vortex flow when the vortex breakdown occupies almost all the domain.

The cyclone happens when the centrifugal force overcome the poloidal Lorentz force, the poloidal flow is totally reversed ($\Gamma \sim 10^{-2}$–1). Although the poloidal flow exists, the dominant flow is mainly in the azimuthal direction. The angular momentum is now smoothly distributed throughout the domain by the poloidal flow and by turbulent diffusion. A very calm region extends along the axis. A continuous increase of azimuthal kinetic energy occurs over the range of Ha $=$ 0 to Ha $=$ 10 (Fig. 12). Simultaneously, the poloidal kinetic energy is up to two order of magnitude lower than that in the tornado and electro-vortex regimes (Fig. 11). However, a further increase of magnetic field magnitude enhances the overall poloidal flow, which is driven by an Ekman pumping mechanism. A minimum can be seen for Ha$>10^{-1}$, and for high currents (S > 10^4).

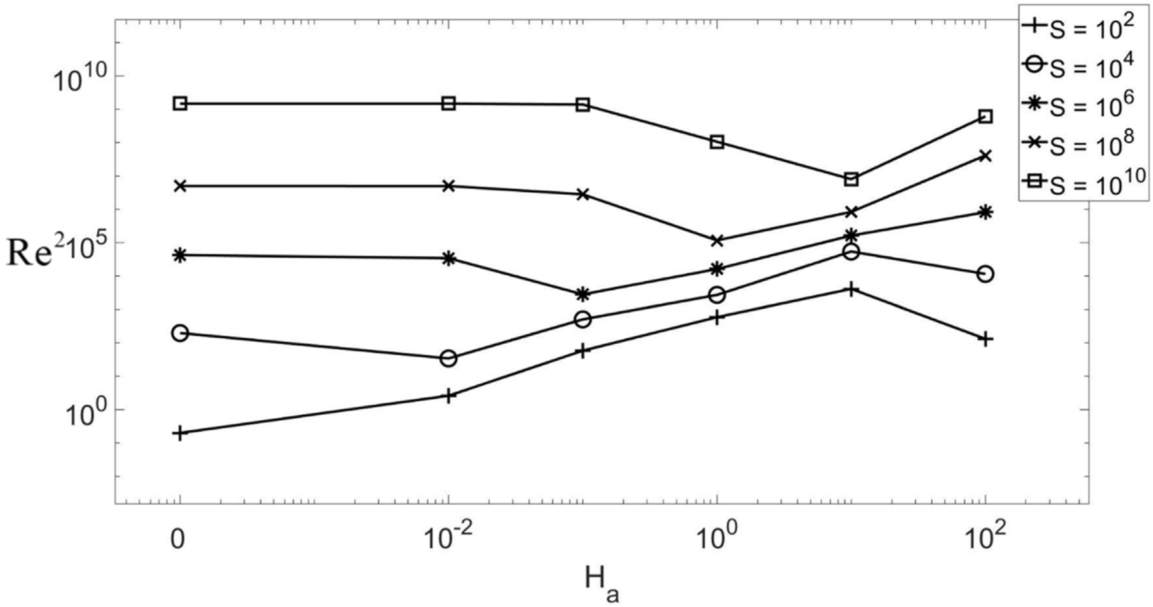

Fig. 11. Volume averaged poloidal kinetic energy inside the fluid domain.

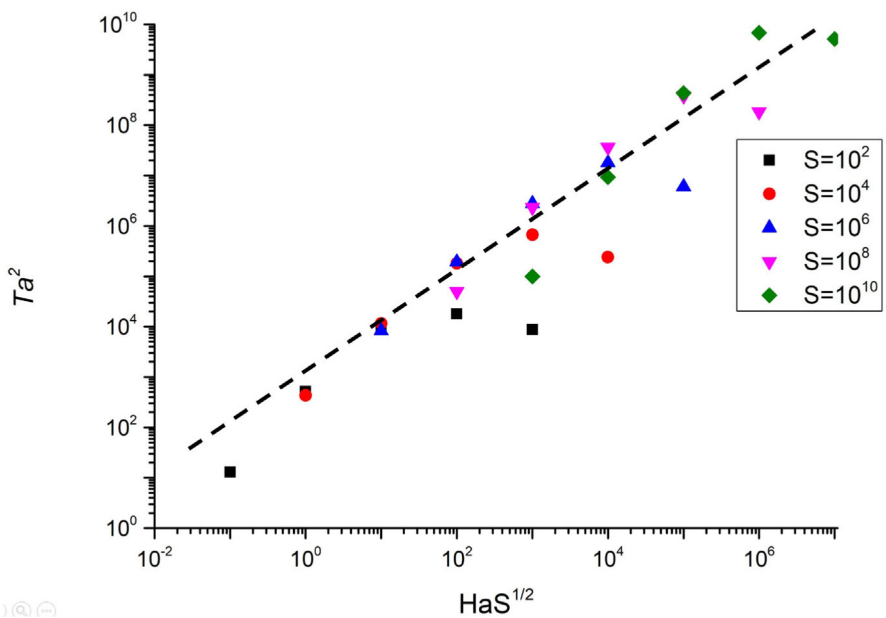

Fig. 12. Volume averaged angular kinetic energy inside the domain.

If Ha is further increased, Ekman pumping can become strong enough so that a swirl confinement can again occur. This time accumulation of swirl emerges within an annulus near the top electrode surface, giving birth to an inverted tornado. Here, a new vortex breakdown also occurs that turns in the same direction as the original electro-vortex. Afterwards, we will see that the induced currents play an important role in the apparition of this inverted tornado. In the electro-vortex, tornado and cyclone flow regimes induced currents are smaller in magnitude than the applied current. In other words, the electric current distribution (Fig. 10) and the poloidal Lorentz force (Figs. 4–7) are sensibly the same as the one without magnetic field (Fig. 10). These induced currents are the strongest where the flow is the strongest. For cyclones and inverse tornados where sufficient swirl accumulation occurs (S<10^8 and H_a >10), the current lines are bent and compressed near the large electrode at the top. Locally, a sufficiently large induced radial current is generated. Interestingly, this compression reduces the effective surface of the top electrode over which the current enters the domain (see Figs. 8 and 10). In this region, the poloidal Lorentz force is no more curl-free (Fig. 8). The prime effect of this compression is to generate a new electro-vortex at the top surface which further support the Ekman driven poloidal flow. This is in accordance with the general understanding that for moderate or high Ha numbers, MHD minimizes Joule heating dissipation by restructuring the flow. Here the restructuration tries to minimize the swirl accumulation by enhancing its evacuation by the poloidal flow. The creation of a new electro-vortex at the top electrode is a crucial ingredient for the generation of the inverse tornado. The flow (vortex breakdown, updraft) and pressure field inside the inverted tornados are very similar to the flow inside tornados encountered for $\Gamma<10^{-2}$. These inverted tornados are developed

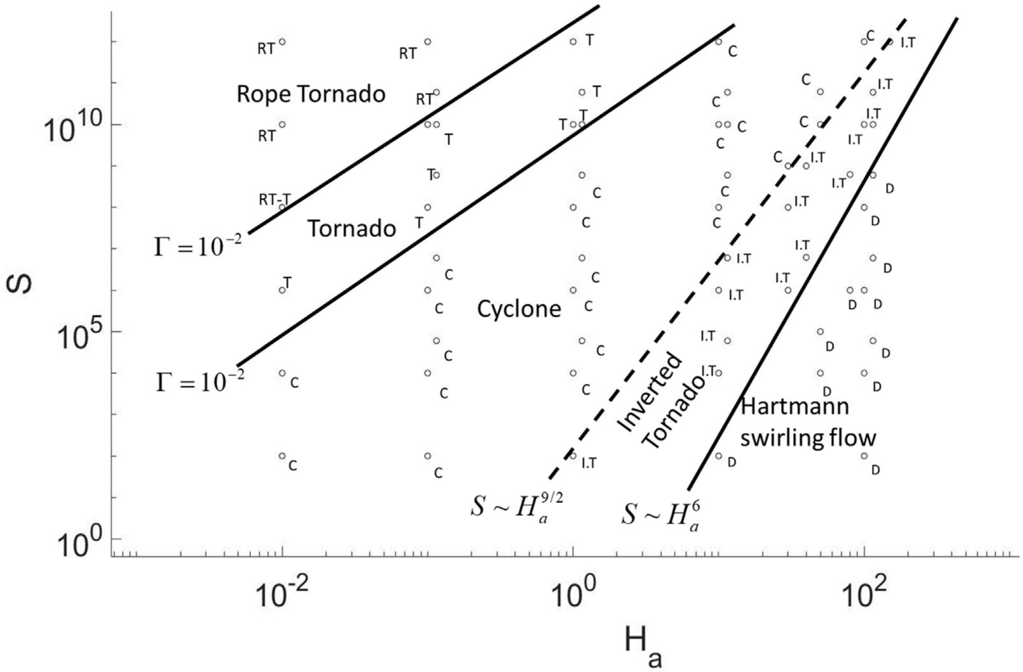

Fig. 13. Flow pattern maps for different S and Ha numbers. (RT): Rope tornado, (T) tornado, (C) cyclone, (IT) inverted tornado, (D) Hartmann swirling flow.

only for large S and large Ha numbers, notice the right top corner of the flow pattern map (Fig. 13).

For large N, the compression of the electric currents lines by the induced currents is much stronger (see $\mathrm{Ha} = 10^2$ for $S<10^6$ in Fig. 10). The electric currents are now flowing almost vertically, further reducing the curl component of the Lorentz force, which results in strong decrease of poloidal flow. A strong damping of the radial and tangential velocity components occurs because of the Hartmann component of the Lorentz force, $\sim -H_a^2 U/P_m$. By comparing Fig. 4 with $\mathrm{Ha} = 10^2$ in Fig. 10, it can be seen that the radial spreading of original current pattern (Ha <<1) has been balanced by the radial induced currents. By reducing the radial currents magnitude, the poloidal Lorentz force becomes curl-free, in addition the angular momentum loses its driving force (see Ha>10). This explains the scaling (Eq. (17)) which is very different from one obtained by [5,36–40]. While in our geometry the current flows between two parallel horizontal electrodes, in [5,36–40] configurations include at least one vertical electrode in which radial currents cannot vanish. There, at high Hartmann numbers the induced currents force the radial current to flow almost entirely inside the Hartmann layer(s). In our configuration, the remaining azimuthal forcing region is located within the bottom Hartmann boundary layer. Inside, the flow experiences less Joule dissipation, giving rise to a thin swirling plane jet flowing radially outward (Fig. 9).

6. Industrial pertinence and conclusion

Depending on the industry and on the properties of the processed material, the parameter S can reach 10^{12}. In the electric arc furnaces, electroslag remelting process, vacuum arc remelting processes and aluminum reduction cells, the applied current ranges from 5k to 150 kA. This current can pass successively through different fluids, such as a plasma, a slag and a liquid metal layers. External magnetic fields in order of a few mTesla are generated by the surrounding electric current lines, or by the presence of neighbor processes. Thus, depending on the size of the electrode (<10 m), Hartmann number can exceed 10^2. Therefore, most the flow predicted in the present study can develop in the industrial processes. As an example in aluminum electrolysis, the presence of gas bubbles all over the electrode induces strong inhomogeneous currents. In the presence of a weak axial magnetic field, it is enough to have a few cm^2 of electrode surface without bubbles to generate locally a electro-vortex, a tornado or a cyclone in the bath region.

Of note, these MHD tornados are mainly driven by the radial and tangential component of the Lorentz force. The development of the MHD tornados is not the fruit of any pulling above the surface as known in the laboratory suction vortexes, here the driving source of the flow field is located at the neck of the tornado. Intriguingly these MHD tornados share very similar features with the atmospheric tornados [32,33], such as the presence of vortex breakdown, low pressures at the surface and downdraft flow inside the core.

The simultaneous application of an electric current and an axial magnetic field generates a large variety of fluid flows. Depending solely on two dimensionless parameters, S and Ha, electro-vortexes, tornado, cyclones, inverted tornado, Hartmann swirling flows are generated. All these flows deserve further studies, especially the transition from one flow regime to another, 3D turbulence and multiphase aspects.

Declaration of competing interest

The authors declare that they have no known competing financial interests or personal relationships that could have appeared to influence the work reported in this paper.

Data availability

The data that supports the findings of this study are available within the article.

Acknowledgments

The authors acknowledge financial support from the Austrian Federal Ministry of Economy, Family and Youth and the National Foundation for Research, Technology and Development within the framework of the Christian-Doppler Laboratory for Metallurgical Applications of Magneto hydrodynamics.

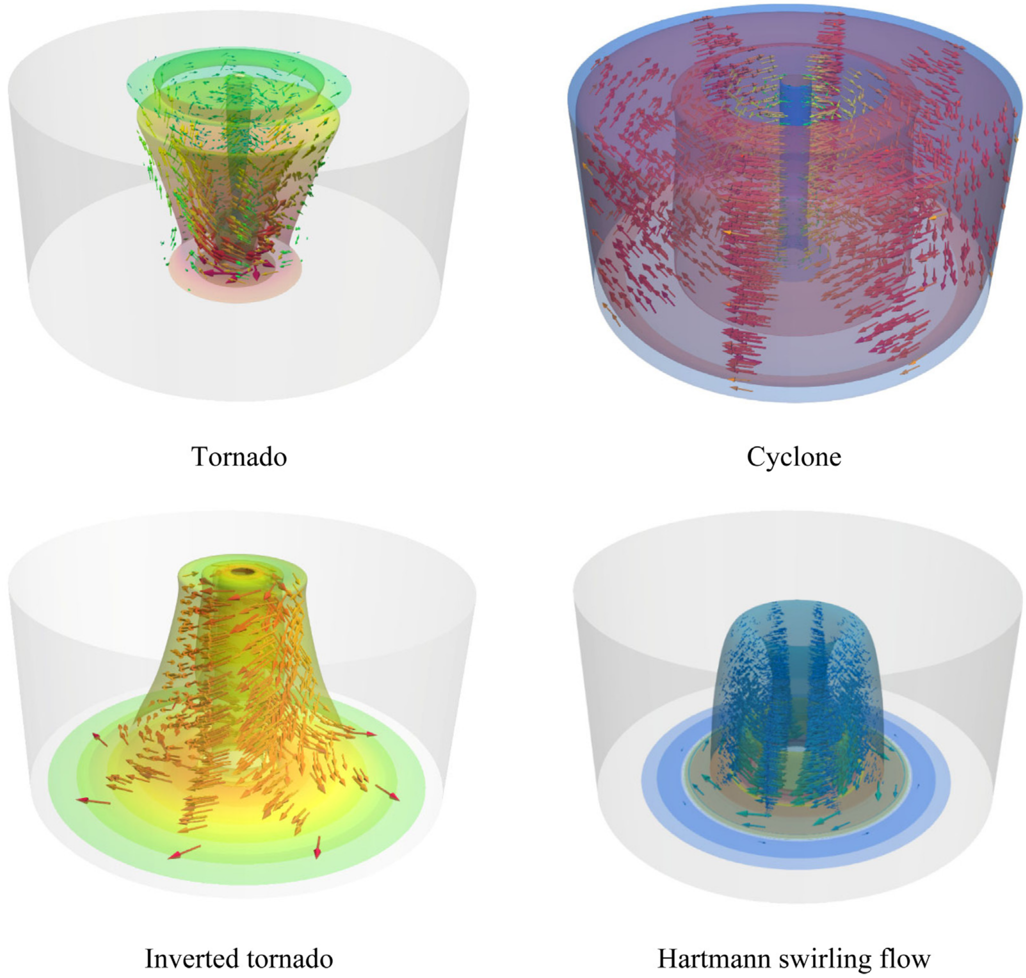

Fig. 14. 3D visualization of the observed flow patterns.

References

[1] V. Bojarevičs, J.A. Freibergs, E.I. Shilova, E.V. Shcherbinin, Electrically Induced Vortical Flows, in: Mechanics of Fluids and Transport Processes, vol. 9, Springer, Dordrecht, 1989, http://dx.doi.org/10.1007/978-94-009-1163-5_8.

[2] G. Antar, A. Lalti, C. Habchi, The spontaneous breaking of axisymmetry in shallow rotating flows, Phys. Fluids 31 (2019) 074104, http://dx.doi.org/10.1063/1.5098367.

[3] J. Pérez-Barrera, G. Ramírez-Zúñiga, E.C. Grespan, S. Cuevas, J.A. del Río, Thermographic visualization of a flow instability in an electromagnetically driven electrolyte layer, Exp. Therm Fluid Sci. 109 (2019) 109882, http://dx.doi.org/10.1016/j.expthermflusci.2019.109882.

[4] J. Perez-Barrera, J. McCloughan, S.A. Suslov, S. Cuevas, Instability of swirling electrolyte flows driven electromagnetically, Magnetohydrodynamics 56 (2–3) (2020) 139–148, http://dx.doi.org/10.22364/mhd.56.2-3.5.

[5] J. Sommeria, Electrically driven vortices in a strong magnetic field, J. Fluid Mech. 189 (1988) 553–569, http://dx.doi.org/10.1017/S0022112088001144.

[6] J. Sommeria, Two-dimensional turbulence, in: Lesieur M., Yaglom A., David F. (Eds.), New Trends in Turbulence Turbulence: Nouveaux Aspects. Les Houches - Ecole D'Ete de Physique Theorique, Vol. 74, Springer, Berlin, Heidelberg, 2001, http://dx.doi.org/10.1007/3-540-45674-0_8.

[7] K. Messadek, R. Moreau, An experimental investigation of MHD quasi-two-dimensional turbulent shear flows, J. Fluid Mech. 456 (2002) 137–159, http://dx.doi.org/10.1017/S0022112001007716.

[8] B. Mahfoud, A. Bendjagloli, R. Bessaïh, Magneto-hydrodynamic co-rotating flow in a vertical cylindrical container, Numer. Heat Transfer A 69 (2016) 1051–1106, http://dx.doi.org/10.1080/10407782.2015.1109383.

[9] B. Mahfoud, R. Bessaïh, Magnetohydrodynamic counter-rotating flow in a cylindrical cavity, Int. J. Heat Mass Transfer 93 (2016) 175–185, http://dx.doi.org/10.1016/j.ijheatmasstransfer.2015.10.009.

[10] B. Gallet, M. Berhanu, M. Mordant, Influence of an external magnetic field on forced turbulence in a swirling flow of liquid metal, Phys. Fluids 21 (8) (2009) 085107, http://dx.doi.org/10.1063/1.3194304.

[11] Y. Yu, B. Li, A. Thess, The effect of a uniform magnetic field on vortex breakdown in a cylinder with rotating upper lid, Comput. & Fluids 88 (2013) 510–523, http://dx.doi.org/10.1016/j.compfluid.2013.10.006.

[12] A. Kharicha, A. Alemany, D. Bornas, Influence of the magnetic field and the conductance ratio on the mass transfer rotating lid driven flow, Int. J. Heat Mass Transfer 47 (2004) 1997–2014, http://dx.doi.org/10.1016/j.ijheatmasstransfer.2003.02.001.

[13] A. Laouari, B. Mahfoud, R. Bessaïh, A. Hadjadj, Hydrodynamic instabilities in swirling flow under axial magnetic field, Eur. J. Mech. - B/Fluids (ISSN: 0997-7546) 85 (2021) 245–260, http://dx.doi.org/10.1016/j.euromechflu.2020.08.006.

[14] A. Jardy, D. Ablitzer, J.F. Wadier, Magnetohydrodynamic and thermal behavior of electroslag remelting slags, Metall. Trans. B 22 (1991) 111–120, http://dx.doi.org/10.1007/BF02672532.

[15] A. Kharicha, E. Karimi-Sibaki, M.H. Wu, A. Ludwig, J. Bohacek, Review on modeling and simulation of electroslag remelting, Steel Res. Int. 89 (1) (2018) 1700100, http://dx.doi.org/10.1002/srin.201700100.

[16] O. Kazak, Modeling of vortex flows in direct current (DC) electric arc furnace with different bottom electrode positions, Metall. Mater. Trans. B 44 (2013) 1243–1250, http://dx.doi.org/10.1007/s11663-013-9899-4.

[17] H. Barati, A. Kharicha, M. Al-Nasser, D. Kreuzer, G. Hackl, M. Gruber, A. Ishmurzin, C. Redl, A. Teplyakov, I. Ludwig, MHD instability at the cathode spot as the origin of the vortex formation in high-intensity plasma arcs, J. Phys. Commun. 6 (2022) http://dx.doi.org/10.1088/2399-6528/ac4b49.

[18] J. Szekely, J. McKelliget, M. Choudhary, Heat-transfer fluid flow and bath circulation in electric-arc furnaces and DC plasma furnaces, Ironmak. Steelmak. 10 (4) (1983) 169–179.

[19] V. Bojarevics, MHD of aluminium cells with the effect of channels and cathode perturbation elements, in: B.A. Sadler (Ed.), in: Light Metals. The Minerals, Metals & Materials Series, Springer, 2003, http://dx.doi.org/10.1007/978-3-319-65136-1_104.

[20] F. Stefani, V. Galindo, C. Kasprzyk, S. Landgraf, M. Seilmayer, M. Starace, N. Weber, T. Weier, Magnetohydrodynamic effects in liquid metal batteries,

IOP Conf. Ser. Mater. Sci Eng. 143 (1) (2016) 012024, http://dx.doi.org/10.1088/1757-899X/143/1/012024.

[21] J.A. Shercliff, Fluid motions due to an electric current source, J. Fluid Mech. 40 (2) (1970) 241–250.

[22] V. Bojarevics, E.V. Scherbinin, Azimuthal rotation in the axisymmetric meridional flow due to an electric-current source, J. Fluid Mech. 126 (1983) 413–430.

[23] A. Kharicha, M. Wu, A. Ludwig, E. Karimi-Sibaki, Influence of the earth magnetic field on electrically induced flows, J. Iron Steel Res. Int. 19 (1) (2012) 63–66, http://ksuxk.cqvip.com/asset/detail/0/20377342831.

[24] A. Kharicha, I. Teplyakov, Yu Ivochkin, M. Wu, A. Ludwig, A. Guseva, Experimental and numerical analysis of free surface deformation in an electrically driven flow, Exp. Therm Fluid Sci. (ISSN: 0894-1777) 62 (2015) 192–201, http://dx.doi.org/10.1016/j.expthermflusci.2014.11.014.

[25] D.A. Vinogradov, I.O. Teplyakov, Y.P. Ivochkin, A. Kharicha, On the applicability of the electrodynamic approximation in the simulation of the electrovortex flow in the presence of an external magnetic field, J. Phys. Conf. Ser. 1128 (1) (2018) 012112.

[26] I. Teplyakov, D. Vinogradov, Y. Ivochkin, A. Kharicha, P. Serbin, Applicability of different MHD approximations in electrovortex flow simulation, Magnetohydrodynamics 54 (4) (2018) http://dx.doi.org/10.22364/mhd, (0024-998X).

[27] K. Liu, F. Stefani, N. Weber, T. Weier, B.W. Li, Numerical and experimental investigation of electro-vortex flow in a cylindrical container, Magnetohydrodynamics 56 (1) (2019) 27–42, http://dx.doi.org/10.22364/mhd.56.1.3, 2020.

[28] I. Kolesnichenko, Peter Frick, Vladislav Eltishchev, Sergei Mandrykin, Frank Stefani, Fluids evolution of a strong electrovortex flow in a cylindrical cell, Phys. Rev. 5 (12) (2020) 123703, http://dx.doi.org/10.1103/PhysRevFluids.5.123703.

[29] W. Herreman, C. Nore, P.Z. Ramos, L. Cappanera, J.L. Guermond, N. Weber, Numerical simulation of electrovortex flows in cylindrical fluid layers and liquid metal batteries, Phys. Rev. Fluids 4 (11) (2019) 113702, http://dx.doi.org/10.1103/PhysRevFluids.4.113702.

[30] W. Herreman, C. Nore, L. Cappanera, J.L. Guermond, Efficient mixing by swirling electrovortex flows in liquid metal batteries, J. Fluid Mech. 915 (25) (2021) A17, http://dx.doi.org/10.1017/jfm.2021.79, 2021.

[31] S. Kenjeres, Electromagnetically driven dwarf tornados in turbulent convection, Phys. Fluids 23 (2011) 015103, http://dx.doi.org/10.1063/1.3541817.

[32] Miroslava Kmecova, Ondrej Sikula, Michal Krajcik, Circular free jets: CFD simulations with various turbulence models and their comparison with theoretical solutions IOP conference series: Materials science and engineering, 2019, http://dx.doi.org/10.1088/1757-899X/471/6/062045, 471 (6).

[33] H.J. Lugt, Vortex breakdown in atmospheric columnar vortices, Bull. Am. Meteorol. Soc. 70 (12) (1989) 1526–1537.

[34] R.J. Trapp, 'A clarification of vortex breakdown and tornado genesis', Mon. Weather Rev. 128 (3) (2000) 888–895, http://dx.doi.org/10.1175/1520-0493(2000)128<0888:ACOVBA>2.0.CO;2.

[35] T. Vogt, I. Grants, S. Eckert, G. Gerbeth, Spin-up of a magnetically driven tornado-like vortex, J. Fluid Mech. 736 (2013) 641–662.

[36] J. Boisson, R. Monchaux, S. Aumaître, Inertial regimes in a curved electromagnetically forced flow, J. Fluid Mech. 813 (860) (2017).

[37] Z. Stelzer, S. Miralles, D. Cébron, J. Noir, S. Vantieghem, A. Jackson, Experimental and numerical study of electrically driven magnetohydrodynamic flow in a modified cylindrical annulus. II. Instabilities, Phys. Fluids 27 (2015) 084108.

[38] Z. Stelzer, D. Cébron, S. Miralles, S. Vantieghem, J. Noir, P. Scarfe, A. Jackson, Experimental and numerical study of electrically driven magnetohydrodynamic flow in a modified cylindrical annulus. I. base flow, Phys. Fluids 27 (2015) 077101.

[39] A. Pothérat, Three-dimensionality in quasi two-dimensional flows: Recirculations and barrel effects, Europhys. Lett. 98 (64003) (2012).

[40] A. Poyé, O. Agullo, N.s Plihon, W.J.T. Bos, V. Désangles, Bousselin, G, Scaling laws in axisymmetric magnetohydrodynamic duct flows, Phys. Rev. Fluids 5 (4) (2020) 043701.